Growth of oriented Bi nanorods at graphite step-edges

Shelley A. Scott,[1] Milo V. Kral,[2] and Simon A. Brown[1,*]
[1]*The MacDiarmid Institute for Advanced Materials and Nanotechnology, Department of Physics and Astronomy, University of Canterbury, Christchurch, New Zealand*
[2]*Department of Mechanical Engineering, University of Canterbury, Christchurch, New Zealand*
(Received 25 July 2005; published 15 November 2005)

We report on the growth of ordered arrays of bismuth nanorods, extending outward from highly oriented pyrolitic-graphite (HOPG) step–edges. The rods grow via adatom diffusion in a multilayer two-dimensional growth mode, with $\{01\bar{1}2\}_{\mathrm{Bi}}$ planes parallel to the basal plane of the substrate, and in-plane orientations aligned with the high symmetry directions of the substrate such that $\langle 11\bar{2}0\rangle_{\mathrm{Bi}} \| \langle 10\bar{1}0\rangle_{\mathrm{HOPG}}$. The morphologies are characterized with varying particle flux and coverage. It is shown that bismuth aggregates become elongated when the particle flux is reduced. When coupled with an anisotropic diffusion field surrounding step-edge structures, this results in the manifestation of rods in a low flux growth environment. The rods are only ~2 nm tall and can extend up to several microns in length.

DOI: 10.1103/PhysRevB.72.205423 PACS number(s): 81.16.Rf, 64.70.Nd, 68.43.Jk, 81.05.Bx

I. INTRODUCTION

The growth of nanoscale surface structures from the vapor phase has enjoyed many decades of active research. The driving force for this pursuit in recent years, is undoubtedly tied to their potential for exploitation in next generation electronic, optical, and catalytic devices. Of particular interest are materials whose physical properties are enhanced by such a reduction in size. Bismuth is a group V semimetal with a carrier density five orders of magnitude lower than in most metals, and a Fermi wavelength in the order of tens of nanometers. These unusual electronic properties provide for an attractive case study for quantum transport and finite size effects.[1] Desirable properties such as superconductivity,[2] increased magnetoresistance,[3] and enhanced thermoelectric efficiency[4] have been observed in bismuth nanostructures, leading to extensive interest in their fabrication. Nanowires have been fabricated by electrodeposition[5] and templated cluster assembly[6] techniques, and nanotubes produced by solvothermal methods.[7] Also, the growth of thin bismuth films have been studied on substrates such as mica,[8] $BaF_2(111)$,[9] Si(111),[10] and GaSb(110).[11]

Highly ordered pyrolitic graphite (HOPG) has been extensively used as a substrate for investigating diffusion mediated island growth processes.[12,13] Its appeal lies in its atomically smooth and weakly interacting nature,[14] which allows for high adatom mobilities and abrupt adsorbate/substrate interfaces.[15] Additionally, the substrate cleaving process introduces step-edges, which provide large arrays of linear defect traps for diffusing adatoms.[16] This so-called step-edge decoration is well known and has been utilized to enable self-assembly of nanowire-type structures *parallel* to the step-edges, from a range of materials, using a variety of deposition techniques.[17,18]

Typically, decoration of HOPG step-edges is characterized by the nucleation of relatively compact clusters, which bear a resemblance to those aggregated on the flat terraces between the step-edges.[19–21] We report here on the growth of large scale networks of ordered bismuth nanorods extending *outward* from the HOPG step-edges. The morphology is characterized with varying coverage and flux, and the growth is discussed in terms of the crystallography of the rods and established models of diffusion limited aggregation (DLA).[22]

II. EXPERIMENT

Thin Bi films were prepared by vapor deposition in an ultrahigh vacuum (UHV) chamber, with a base pressure of 10^{-10} Torr attained via ion pumping. Grade STM-1 HOPG substrates (Structure Probe, Inc.) were cleaved in air with adhesive tape, mechanically mounted to an oxygen-free high conductivity copper sample holder, and immediately loaded into the UHV chamber. The substrates were shielded from back streaming ions from the ion pump, which have been shown to introduce surface defects.[23] Residual surface contaminants were removed by thermal treatment under UHV at ~720 K with a 50 W UV lamp mounted inside a heat shielded tantalum oven, for at least 12 h. High purity (99.998%) Bi was thermally evaporated from an alumina coated tungsten crucible (Midwest Tungsten Supplies) at a distance of 25 cm from the sample holder and deposited on the substrates at room temperature. The deposition rate (flux) and deposited dose (coverage) were monitored with a calibrated quartz crystal microbalance. The flux and coverage are measured in units of monolayers (ML), where 1 ML is equivalent to the average atomic spacing in bulk Bi (3.4 Å). Samples were prepared for the flux range, 7×10^{-4}–0.2 Å/s, and coverages between 0.2 ML and 1.5 ML (at higher coverages, the rod structures of interest in this paper become obscured by the onset of film growth, although a 12 ML sample was used for structure determination). The chamber was vented with dry nitrogen 1 h after deposition and the samples removed for *ex situ* analysis.

The surface morphologies were investigated with scanning electron microscopy (SEM) using a JEOL JSM6100 instrument with an accelerating voltage set to 8 kV to minimize sample damage. Higher spatial resolution and height data were obtained with an atomic force microscope (AFM)

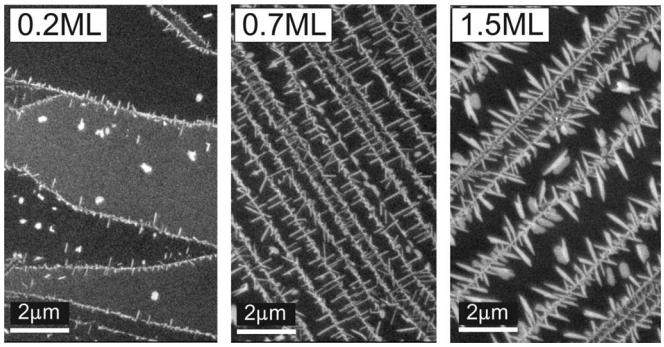

FIG. 1. Representative SEM images of the evolution of step-edge morphology with increasing coverage in the low flux regime. The coverage is indicated on the images, the flux is held constant at 0.005 Å/s.

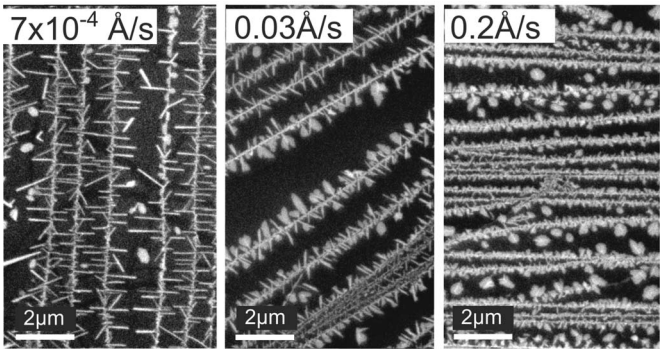

FIG. 2. Representative SEM images of the evolution of step-edge morphology with increasing flux. The flux is indicated on the images, the coverage is held constant at 1.5 ML.

in tapping mode (Digital Instruments Dimension 3100). The AFM probe tips were etched silicon-type NSC14 from Micro-Masch.

The crystallographic orientation of the bismuth aggregates and HOPG substrates was obtained with electron backscatter diffraction (EBSD), using an HKL Nordlys detector and CHANNEL5 software. EBSD is a SEM-based technique, which produces diffraction patterns of backscattered Kikuchi bands from a crystal surface[24] tilted at 70° to the electron beam. The CHANNEL5 software analyzes the patterns and suggests orientation solutions (indexes) ranked in ascending order of mean angular deviation (MAD), which is an indicator of how well the experimental pattern fits a model solution. Typically, a MAD <1 is considered acceptable for accurate solutions. In this study, we accepted solutions in the MAD range 0.2–0.8. The appeal of EBSD lies in its ability to correlate crystal lattice orientation (with respect to a reference axis) with the morphology recorded in the SEM images.

III. RESULTS AND DISCUSSION

A. SEM morphologies

Representative SEM images showing the evolution of film morphology with increasing coverage are presented in Fig. 1 for a fixed flux of 0.005 Å/s. The 0.2 ML image shows step-edge decoration with little island nucleation on the terraces between the steps, which is evidence of high adatom mobility on the HOPG surface. It is apparent that small rod-like structures protrude from the step-edges. The 0.7 ML SEM image shows an increased prominence of the rods, and it is also clear that they are well oriented, producing ordered arrays of Bi nanorods at the step-edges (the orientation will be discussed further in Sec. III C). The 1.5 ML image shows a general increase in the size of the rods.

The evolution of the rod morphology as a function of increasing flux (coverage fixed at 1.5 ML) is shown in Fig. 2. The 7×10^{-4} Å/s flux image shows extremely elongated rod shaped islands extending from the step-edges. A high degree of order in their orientation is again evident. When the flux is increased to 0.03 Å/s, the rods generally become shorter and broader. A further increase to 0.2 Å/s produces a markedly more compact step-edge decoration, with little evidence of the rod structures. Increasing the flux results in a morphology transition from rod-like to compact structures aggregated along the step-edges.

A previous study of the Bi/HOPG system,[25] in which the substrates were not thermally cleaned prior to deposition, did not observe this morphology. Instead, a high density of small, slightly elongated structures were observed on the graphite terraces. Substrate preparation has been shown to be a critical step in obtaining high adatom mobility[23] on HOPG, and indeed, this ordered rod-like morphology does not manifest itself when the heating step is omitted from the substrate preparation procedure in the present study.

Quantitative data on the dimensions of the step-edge aggregates was obtained from AFM scans, which provide better resolution than SEM imaging for small scan areas. Representative AFM images are shown in Fig. 3. Fluxes of 0.005 Å/s [Figs. 3(a)–3(c)] and 0.2 Å/s [Fig. 3(e)] have been chosen as examples of the low and high flux regimes, respectively. The rod height data shown in Fig. 3 will be discussed in more detail below; we focus now on the length and width data.

The degree of aggregate elongation is defined here by the aspect ratio (length/width). AFM images similar to those in Fig. 3 have been used to calculate histograms of the aggregate length and aspect ratio, which are shown in Figs. 4(a) and 4(b) for coverages of 0.2 ML, 0.7 ML, and 1.5 ML, in the low flux regime. These plots show a broad distribution of both lengths and aspect ratios. The tails on the distributions show that some rods are significantly longer and more elongated than the general population. The longest rods are of order 2.5 μm long in the 1.5 ML coverage sample, and the aspect ratio can be as high as 20 for some structures.

Figures 5(a) and 5(b) show plots of the step-edge aggregates' mean length and width as a function of increasing coverage for low (0.005 Å/s, open symbols) and high (0.2 Å/s, closed symbols) fluxes. Each plotted point is composed of measurements taken from multiple regions of the sample, and in some cases multiple samples, to ensure a representative data set. Figure 5(a) shows that the mean rod length increases with increasing coverage for both fluxes. From this plot, it is evident that, for a given coverage, the mean length of rods grown in a low flux environment is greater than for aggregates grown in the high flux regime. From the linear fits to the data in Fig. 3 (and converting

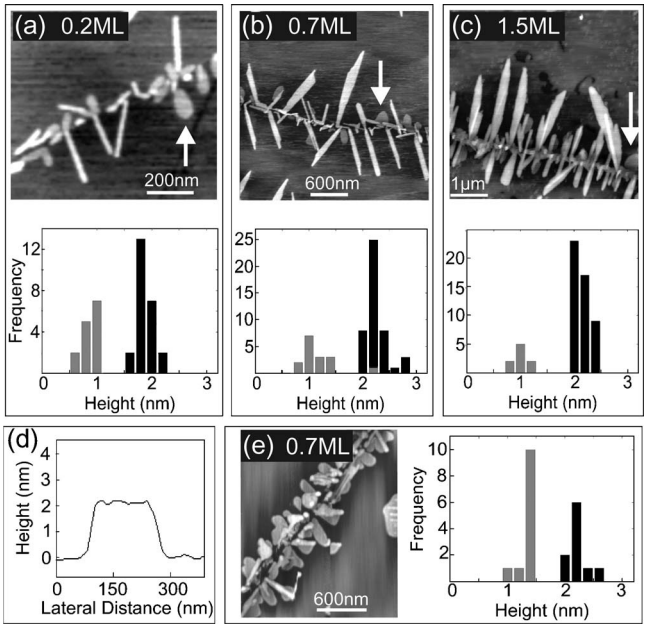

FIG. 3. Representative AFM images of step-edge structures and histograms of the aggregate heights, the black bars in the histogram represent the rod morphologies, while the gray bars represent the smaller broader aggregates which are indicated with an arrow in the AFM images. (a)–(c) show increasing coverage at a constant flux of 0.005 Å/s. (d) Shows AFM height cross section through the largest rod in (b) (center of image, above the step-edge). (e) Image and histogram for a 0.7 ML coverage sample, flux=0.2 Å/s.

coverage into the deposition time domain), the mean growth rates for the low flux rod lengths are 1.2 ± 0.5 nm/s, considerably less than that of high flux aggregates which grow at 26 ± 5 nm/s. Figure 5(b) shows that the mean aggregate width also increases with increasing coverage for both flux regimes, with a growth rate of 0.2 ± 0.1 nm/s and 17 ± 5 nm/s for the low and high flux regimes, respectively. Therefore, it is clear that rod-type structures develop only in the low flux regime, where the aggregates' growth rate is significantly less than in the high flux regime.

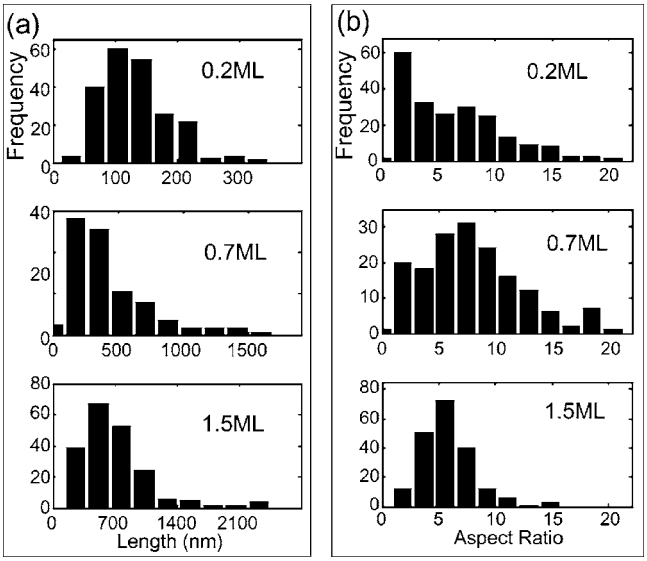

FIG. 4. Histograms of the step-edge aggregate length (a) and aspect ratio (length/width) (b) for the low flux (0.005 Å/s) regime; the coverage is indicated on each histogram.

Figure 5(c) shows the mean aspect ratio as a function of increasing coverage for both high fluxes and low fluxes and indicates that there is no distinguishable dependence of the degree of elongation on coverage for both flux regimes. It is also obvious from this plot that the mean aspect ratio is significantly greater for step-edge structures grown in a low flux environment (7 ± 1) compared to their high flux counterparts (2.0 ± 0.3). These two observations lead to the conclusion that the degree of elongation is approximately independent of the amount of material deposited and depends only on the particle flux.

B. Rod heights

Height histograms (with AFM images) are shown in Figs. 3(a)–3(c) for step-edge aggregates grown in the low flux environment (since this is where the rod shapes are most pronounced) for a range of coverages. The AFM images show that the step-edge decoration is composed of both rod-like structures and, occasionally, more compact morphologies (indicated with arrows in the AFM images). The black bars in the histogram represent height data taken from the rods, and the gray bars show heights for the smaller broader (arrowed) structures. Figures 3(a)–3(c) show that the rod height is of order 2 nm tall, and the smaller aggregates are of order 1 nm tall. On average, at least 90% of the aggregated material contributes to the growth of rod structures (rather than the smaller broader aggregates). The heights (for both rods and broader structures) remain approximately constant with increasing coverage, within the range 0.2–1.5 ML, indicating a two-dimensional growth mode. The AFM height cross section through a rod in Fig. 3(d) demonstrates the uniform height of the aggregates. Therefore, with increasing coverage, the rods grow in both length and width while keeping a relatively constant aspect ratio, but maintain a constant height of ~2 nm.

An AFM image and height histogram are shown in Fig. 3(e) for a high flux sample at a coverage of 0.7 ML. The AFM image reveals mainly compact structures, which are again of order 1 nm in height, as shown in the accompanying histogram. The histogram shows a population of taller structures, which are typically small rod-like structures which form part of broader aggregates (as can be seen in the AFM image), rather than the well-defined, isolated rods found in the low flux regime. Therefore, it is clear that well-defined rod growth is only achieved in the low flux environment.

C. Crystallographic orientation

Bismuth has a rhombohedral crystal structure (space group $R3\bar{m}$), with two atoms per unit cell, and a bulk lattice constant of 4.75 Å. The axial angle is 57.35° and the basis atoms are located at (0,0,0) and (0.474,0.474,0.474).[26] The structure is composed of puckered layers of covalently bonded atoms stacked in layers perpendicular to the trigonal axis.[27] Each atom has three nearest neighbors (3.1 Å) in the

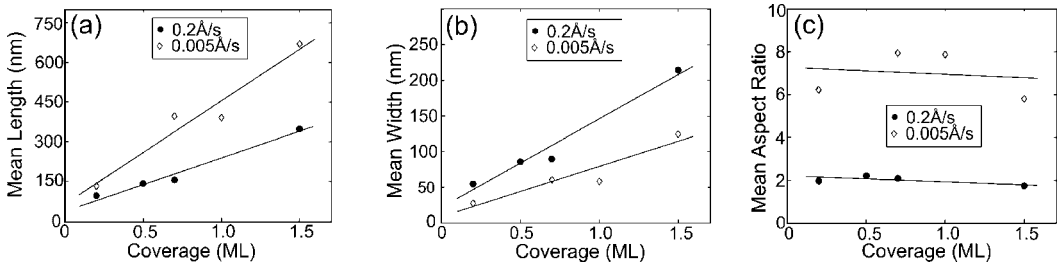

FIG. 5. Plots of the mean step-edge aggregate length (a), width (b), and aspect ratio (length/width) (c), data as a function of increasing coverage, for the coverage range 0.2–1.5 ML. Two flux regimes are plotted (indicated in the legends). The solid lines are least squares fits to the data.

same layer (covalent intralayer bonds) and three next-nearest neighbors (3.5 Å) in the adjacent layer (weaker interlayer bonds). The crystal symmetry can also be visualized within a hexagonal basis, as shown in Fig. 6(a), where a {0001} plane and a $\{01\bar{1}2\}$ plane are shaded dark gray and light gray, respectively. The $\{01\bar{1}2\}$ lattice mesh (which will be used in the following discussion of results) is illustrated in Fig. 6(b) with the covalent intralayer bonds indicated by solid lines and the weaker interlayer bonds represented by dashed lines. Note that we adopt exclusively the hexagonal labeling system; however, rhombohedral and pseudocubic coordinate systems are also used extensively in the literature and a conversion table (along with a more comprehensive account of the crystal structure) is available.[27]

Determination of the crystallographic orientation of terrace nucleated islands in the Bi/HOPG system is described in detail elsewhere.[28] We present here a summary for the specific case of the step-edge structures. The EBSD technique requires that aggregates are thick enough to accommodate the interaction volume of the divergent electron beam. Consequently, the rod structures were too thin to produce an EBSP for bismuth. However, Kikuchi patterns could be obtained for step-edge structures from a 12 ML coverage film, which corresponds to a deposited dose of 4.1 nm, aggregated into closely packed structures ~5–7 nm tall.

Figure 7(a) shows a representative field-emission SEM (FE-SEM) image of step-edge decoration from a 12 ML film. Note that the image resolution is poor because optimum microscope parameters for obtaining EBSPs did not coincide with optimum SEM imaging settings. A higher resolution AFM image of the same sample is shown in Fig. 7(b), in which the elongated step-edge structures can be clearly observed in the center of the image. The direction of aggregate elongation has been shown to be parallel to the stripes which are observed on the surface of the aggregates.[28] The arrowed line in Fig. 7(a) serves to represent the stripe direction and, hence, the direction of aggregate elongation in this image.

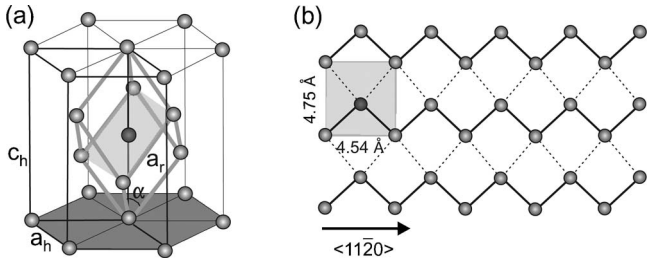

FIG. 6. (a) Rhombohedral Bi structure (a_r=4.75 Å, α=57.35°) superimposed within a hexagonal basis (a_h=4.54 Å, c_h=11.86 Å). A {0001} plane and a $\{01\bar{1}2\}$ plane are shaded dark and light gray, respectively. (b) The $\{01\bar{1}2\}$ lattice mesh with a $\{01\bar{1}2\}$ unit cell shaded. The solid lines indicate the strong intralayer (covalent) bonds and the dashed lines represent the weaker interlayer bonds.

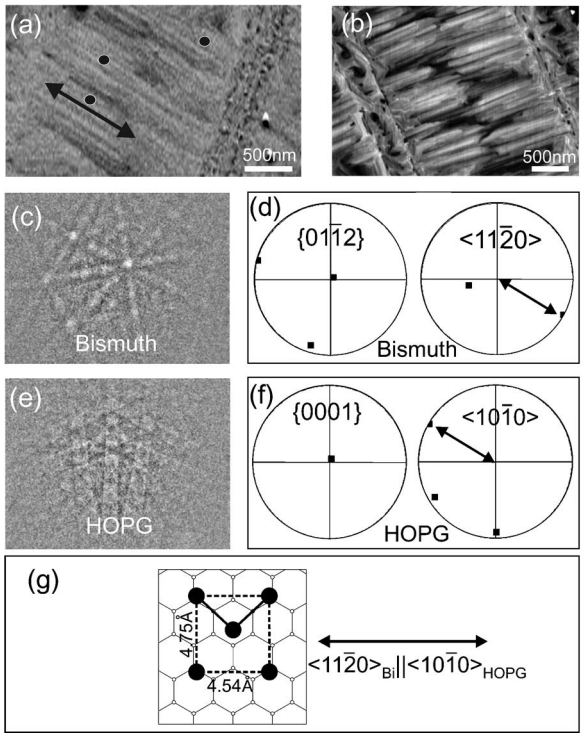

FIG. 7. EBSD determination of the crystallographic orientation. (a) FE-SEM image of a 12 ML coverage film showing structures protruding from a step-edge (right in the image), the black circles indicate sites where local EBSD probing of the films orientation was performed, the arrowed line shows the direction of the stripes. (b) An AFM image showing higher resolution of the 12 ML step-edge structures. (c) Representative bismuth EBSP obtained from the image in (a). (d) Bismuth EBSD pole figures, the arrowed line is a superposition of the stripe direction from (a). (e) Typical graphite EBSP. (f) Graphite EBSP pole figures, with the stripe direction from (a) superimposed. (g) Schematic representation of the preferred adsorbate/substrate orientation with the growth direction indicated.

The black dots indicate sites where the structure was probed with the electron beam.

A typical EBSP from a 12 ML Bi film is shown in Fig. 7(c), and the index solutions are presented in the pole figures in Fig. 7(d). The $\{01\bar{1}2\}$ pole figure (stereographic projection of crystallographic plane normals) shows that the aggregates are oriented with $\{01\bar{1}2\}$ planes parallel to the surface plane. The $\langle 11\bar{2}0\rangle$ pole figure (stereographic projection of crystallographic directions) has the arrow from the SEM image superimposed and shows that the stripe direction coincides with a $\langle 11\bar{2}0\rangle$ pole, revealing that the aggregates are elongated along a $\langle 11\bar{2}0\rangle_{\mathrm{Bi}}$ direction.

The substrate orientation was probed either between the aggregates or by penetration of the electrons through thin regions of the Bi film. Figure 7(e) shows an EBSP from the HOPG substrate, and the associated pole figures are shown in Fig. 7(f) with the island stripe direction also superimposed. The $\langle 10\bar{1}0\rangle_{\mathrm{HOPG}}$ pole figure shows an alignment of the stripe (and hence elongation) direction with a $\langle 10\bar{1}0\rangle_{\mathrm{HOPG}}$ direction. This aggregate/substrate orientation relationship was found for approximately 90% of indexing.

Therefore, it is clear that the preferred rod orientation is defined by $\{01\bar{1}2\}_{\mathrm{Bi}}\|\{0001\}_{\mathrm{HOPG}}$ and $\langle 11\bar{2}0\rangle_{\mathrm{Bi}}\|\langle 10\bar{1}0\rangle_{\mathrm{HOPG}}$. Figure 7(g) shows the preferred orientation of the $\{01\bar{1}2\}_{\mathrm{Bi}}$ lattice on the graphite substrate (the positions of the Bi atoms with respect to the substrate carbon atoms are defined arbitrarily with regard to surface translation). Understanding the preferred orientation in terms of the adsorbate/substrate misfit is complicated by the second basis atom (which is slightly off center in the $\{01\bar{1}2\}$ unit cell). The $\langle 11\bar{2}0\rangle_{\mathrm{Bi}}\|\langle 10\bar{1}0\rangle_{\mathrm{HOPG}}$ orientation gives a misfit of -7.7% parallel to the growth direction ($\langle 11\bar{2}0\rangle_{\mathrm{Bi}}$ and the short edge of the unit cell) and $+11.5\%$ perpendicular to the growth direction. It should be noted, however, that the azimuthal alignment $\langle 11\bar{2}0\rangle_{\mathrm{Bi}}\|\langle 11\bar{2}0\rangle_{\mathrm{HOPG}}$ would produce a smaller misfit in both directions. Azimuthal orientations which do not favor a minimum misfit have been observed in the Pd/graphite system,[29] and attributed to a preference for adsorbate bonding over β sites of the graphite lattice. However, the site bonding preferences for bismuth on the graphite lattice are not known.

The alignment of the rods with a high symmetry direction of the substrate, accounts for the ordering at the step-edges observed in the SEM images of Fig. 1. In the 0.7 ML image, the majority of rods protrude perpendicularly from the step-edge; while in the 1.5 ML image, the dominant rod orientation is at 60° to the step-edge. This indicates that the HOPG step-edges in these two images are oriented in different crystallographic directions ($\langle 11\bar{2}0\rangle_{\mathrm{HOPG}}$ and $\langle 10\bar{1}0\rangle_{\mathrm{HOPG}}$, respectively). It is also interesting to note that a 30° rotation is the most common misorientation of the rods with respect to the preferred orientation (as can be seen in the SEM and AFM images, where an array of rods perpendicular to the step-edge has occasional rods oriented at 60°), which corresponds to $\langle 11\bar{2}0\rangle_{\mathrm{Bi}}\|\langle 11\bar{2}0\rangle_{\mathrm{HOPG}}$.

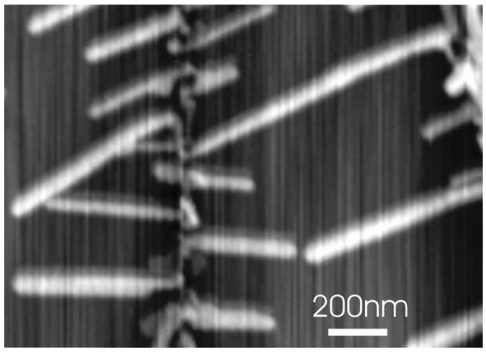

FIG. 8. AFM image showing an example of rods from adjacent step-edges which have grown together to form a continuous structure (this morphology is frequently observed).

D. Growth mechanism

1. Edge diffusion

Pattern formation on surfaces via diffusion, nucleation, and subsequent aggregation of island-type structures is influenced by the relative rate of edge diffusion compared to diffusion across the substrate terraces.[30,31] To maintain a compact morphology, the rate of transport of material around the perimeter of a structure (by edge diffusion and corner crossing) must exceed the arrival rate of new adatoms to the perimeter via random migration on the substrate. Conversely, in the extreme case where edge diffusion is entirely frozen, branched fractal structures aggregate via the classical DLA process.[22] The generally smooth perimeter of the rods in the Bi/HOPG system implies effective adatom transport down the sides, although it should be noted that very large structures [for example, in Fig. 3(c)] do demonstrate a susceptibility to Mullins-Sekerka-type[32] tip instabilities.

Anisotropies in the aggregates' morphology arise when the energy barriers for edge diffusion are higher along some crystallographic directions than others. The elongation of the step-edge aggregates along the $\langle 11\bar{2}0\rangle_{\mathrm{Bi}}$ directions indicates enhanced edge diffusion along these directions. Figure 6(b) illustrates that $\langle 11\bar{2}0\rangle_{\mathrm{Bi}}$ is the direction of the zigzag chains of covalent bonds which characterize the $\{01\bar{1}2\}$ surface lattice. Adatoms diffusing around the perimeter of an aggregate would be more likely to become fixed at the end of a covalent bond chain, hence, extending the structure in the $\langle 11\bar{2}0\rangle_{\mathrm{Bi}}$ direction, rather than affixing to a site adjacent to the chains where the bonding is weaker. Needle growth has been observed for electrodeposition in the Bi/Au(111) system and attributed to faster diffusion along the close packed edges of a rectangular Bi unit cell.[33] This may also play a roll in the Bi/HOPG system, since the zigzag covalent bond chains are also parallel to the short edge of the $\{01\bar{1}2\}$ unit cell.

The effective transport of adatoms from the sides to the tips of the rods is evident also from the existence of rods at neighboring step-edges which have grown together to form a continuous structure, as shown in Fig. 8. Two rods from adjacent step-edges that are almost touching tip-to-tip are fea-

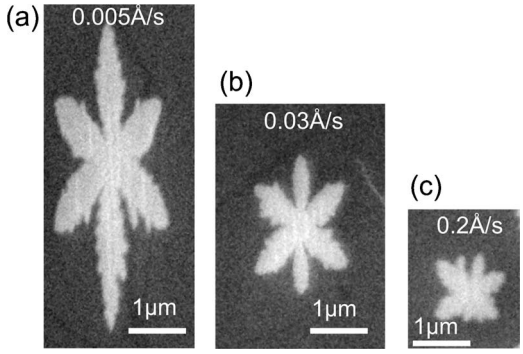

FIG. 9. Representative SEM images of terrace nucleated aggregates showing the evolution in morphology with flux (indicated on the images); coverage is fixed at 1 ML.

tured in the bottom right of the image. Competitive adatom capture rapidly depletes the diffusion field in the region between the two tips, which would normally impose a self-avoiding growth mechanism on the aggregates. The rods can only continue growing toward each other and eventually touch (like the structure in the top right of the same image) if adatoms arriving at the sides of the rods can be transported to the tips.

We now consider the flux dependence of the rod-type growth. To begin, it is useful to consider the flux dependence of terrace nucleated islands, where the diffusion field experienced by an island is relatively isotropic. Figure 9 shows representative SEM images of the evolution in island morphology with increasing flux (at constant coverage). We observe six-pointed star-shaped islands, which are very elongated at low flux (0.005 Å/s). The stars become less elongated with increasing flux, until there is no significant island elongation in the high (0.2 Å/s) flux regime. Note, however, that they do not feature the same extent of elongation (or compact shapes) as the step-edge aggregates. We point out that we are only interested in the elongation here, a detailed study of the morphology of terrace nucleated islands will be presented elsewhere.[34]

EBSD data show that the structure of the star-shaped islands is identical to the case of the rods,[28] i.e., the preferred orientation relationship is $\{01\bar{1}2\}_{\mathrm{Bi}} \| \{0001\}_{\mathrm{HOPG}}$ with $\langle 11\bar{2}0\rangle_{\mathrm{Bi}} \| \langle 10\bar{1}0\rangle_{\mathrm{HOPG}}$, and the direction of island elongation is parallel to $\langle 11\bar{2}0\rangle_{\mathrm{Bi}}$. A reduction in particle flux allows more time for adatoms to overcome edge diffusion barriers (and smooth out the advancing growth front) before the arrival of subsequent adatoms to the island perimeter from the diffusion field. The increasing island elongation with decreasing flux, observed in Fig. 9, implies that the edge diffusion length along $\langle 11\bar{2}0\rangle_{\mathrm{Bi}}$ directions increases with the reduction in flux, resulting in more efficient mass transport in these directions and, hence, island elongation. This tendency for elongation is obscured at higher fluxes by the more rapid arrival rate of new adatoms from the diffusion field, which "pin" the edge adatoms in place, ending their diffusion.

2. Anisotropic diffusion field

For the terrace nucleated islands, we assumed an approximately isotropic diffusion field around the island perimeter.

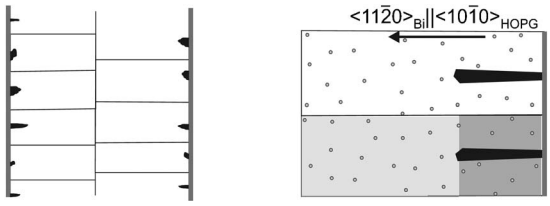

FIG. 10. Schematic illustration of the capture zones surrounding aggregates nucleated on step-edges. The left diagram shows a large scale perspective with the capture zones surrounding each rod. The right illustration shows two adjacent capture zones with diffusing adatoms represented as balls. The light shaded region depicts adatoms that are most likely to arrive at the tips of the rods, while those within the dark shaded regions will likely arrive at the sides of the rods.

However, this is certainly not the case for step-edge aggregates, where a high linear density of aggregates nucleate along the steps (defect decoration). The resulting distorted diffusion field is illustrated in Fig. 10. The left illustration shows small structures nucleated along two step-edges. The rectangles which surround them represent adatom capture zones and are constructed by drawing perpendicular bisectors between neighboring islands. Any adatom deposited within a particular capture zone is most likely to contribute to the growth of the island within it. The drawing to the right depicts the reduced diffusion field between neighboring aggregates, which results from competitive adatom capture. Adatoms within the dark shaded region (in the bottom capture zone) are more likely to arrive at the sides of the rod, while those within the light shaded region will probably impinge near the tip. It is clear that fewer adatoms reach the sides of the rod compared to the tip.

The natural tendency for faster diffusion along $\langle 11\bar{2}0\rangle_{\mathrm{Bi}}$ directions in a low flux environment (as observed in the elongation of the terrace nucleated islands), coupled with a further reduction in local flux arriving to the edges due to competitive adatom capture, results in an exaggeration of the preference for growth in $\langle 11\bar{2}0\rangle_{\mathrm{Bi}}$ directions, producing rod-like morphologies at step-edges in the low flux regime.

E. Step-edge spacing

The local diffusion field, and, hence, the aggregate morphology, is also affected by the spacing between step-edges. Closely spaced steps result in fewer adatoms available per aggregate (competitive capture) and, consequently, slower growth rates. This tends to enhance any elongation, but limits the length of the rods. Widely spaced steps result in an increased rate of adatom impingement to the rod tips (higher local flux), which has a twofold effect. First, the increased number of adatoms allows the growth of longer rods (for example, compare the center step-edges with those at the far right in the 7×10^{-4} Å/s image in Fig. 2). Second, the increased local flux may dominate the growth and cause tip instabilities, hindering elongation. This can be observed in the 0.03 Å/s image in Fig. 2, where the widely spaced center steps show branched growth, while the closely spaced steps

in the bottom of the image feature compact rod shapes. Note, however, that the effect of the step-edge spacing is much smaller than the experimental particle flux (compare images in Fig. 2).

F. Two-dimensional growth

Unlike semiconductor surfaces, there are no dangling bonds on the clean HOPG basal plane and growth proceeds with van der Waals forces to the surface.[15] Consequently, three-dimensional growth is usually observed for large islands on graphite at room temperature (for example, Sb, which is structurally very similar to Bi, aggregates into three-dimensional islands[35] on HOPG). Weak interface bonding was certainly observed in the Bi/HOPG system; difficulties with AFM imaging were encountered due to a tendency for the structures to crumble and move relative to the substrate under the cantilever tip. The two-dimensional growth in the present case indicates a high barrier for adatom migration from the side faces to the top face of the structure (Ehrlich-Schwoebel-type[36] barrier) for $\{01\bar{1}2\}$ islands. This is also found in the Au/HOPG system, which features the aggregation of very flat islands[13] (heights comparable to the present case of bismuth rods).

The growth of multilayer two-dimensional islands, which exhibit preferred heights, has been observed in several adsorbate/substrate systems,[37,38] where the phenomenon was attributed to a quantum size effect originating from confinement of electrons in the vertical direction. Recently, a two-dimensional growth mode was reported for the Bi/Si(111) system at room temperature, where $\{01\bar{1}2\}$ island growth proceeded laterally at a constant height of 1.3 nm.[39] Exposure of a $\{01\bar{1}2\}_{\mathrm{Bi}}$ surface requires covalent bond breaking, resulting in 50% of surface atoms supporting a dangling covalent bond. In the Bi/Si(111) system, *ab initio* calculations revealed that the lateral growth of flat topped islands could be accounted for by layer pairing of the $\{01\bar{1}2\}_{\mathrm{Bi}}$ planes, which saturated the dangling covalent bonds,[10,40] rather than by electron confinement. A layer pairing could perhaps account for the lateral rod growth in the Bi/HOPG system; however, we were unable to determine if even atomic layer heights were favored, due to signal noise in the AFM height measurements. Certainly the mean rod height of 2.2 ± 0.4 nm observed in this work is not consistent with the thickness of islands in Ref. 10. Regardless of the precise mechanism, the multilayer two-dimensional growth results in the formation of structures with lateral dimensions orders of magnitude greater than the thickness.

IV. CONCLUSIONS

Our SEM, AFM, and EBSD analysis of step-edge decoration in the Bi/HOPG system has revealed the formation of large arrays of oriented nanorods in the low flux growth regime. With increasing coverage, the rods grow in both length and width with a constant length/width ratio, but maintain a uniform height of $\sim$2 nm within the range 0.2–1.5 ML. The preferred orientation relationship is defined by $\{01\bar{1}2\}_{\mathrm{Bi}}\|\{0001\}_{\mathrm{HOPG}}$ and $\langle 11\bar{2}0\rangle_{\mathrm{Bi}}\|\langle 10\bar{1}0\rangle_{\mathrm{HOPG}}$, with this alignment of the rods with the high symmetry directions of the substrate producing the ordering at the step-edges. The growth mechanism was described within the context of DLA-like processes and edge diffusion, where a tendency for more efficient mass transport along $\langle 11\bar{2}0\rangle_{\mathrm{Bi}}$ directions, coupled with an anisotropic diffusion field surrounding the step-edge aggregates, results in rod growth in a low flux environment.

*Corresponding author. Electronic address: simon.brown@canterbury.ac.nz

[1] Z. B. Zhang, X. Sun, M. S. Dresselhaus, J. Y. Ying, and J. Heremans, Phys. Rev. B **61**, 4850 (2000).
[2] B. Weitzel and H. Micklitz, Phys. Rev. Lett. **66**, 385 (1991).
[3] S. Cho, Y. Kim, A. Freeman, G. Wong, J. Ketterson, L. Olafsen, I. Vurgaftman, J. Meyer, and C. Hoffman, Appl. Phys. Lett. **79**, 3651 (2001).
[4] L. Hicks, T. Harman, and M. Dresselhaus, Appl. Phys. Lett. **63**, 3230 (1993).
[5] K. Liu, C. Chien, P. Searson, and K. Zhang, Appl. Phys. Lett. **73**, 1436 (1998).
[6] J. G. Partridge, S. A. Scott, A. D. Dunbar, M. Schulze, S. A. Brown, A. Wurl, and R. J. Blaikie, IEEE Trans. Nanotechnol. **3**, 61 (2004).
[7] X. Liu, J. Zeng, S. Zhang, R. Zheng, X. Liu, and Y. Qian, Chem. Phys. Lett. **374**, 348 (2003).
[8] H. Wang, J. Jing, R. Mallik, H. Chu, and P. Henriksen, J. Cryst. Growth **130**, 571 (1993).
[9] A. Dauscher, A. Jacquot, and B. Lenoir, Appl. Surf. Sci. **186**, 513 (2002).
[10] T. Nagao, J. T. Sadowski, M. Saito, S. Yaginuma, Y. Fujikawa, T. Kogure, T. Ohno, Y. Hasegawa, S. Hasegawa, and T. Sakurai, Phys. Rev. Lett. **93**, 105501 (2004).
[11] T. van Gemmeren, L. Lottermoser, G. Falkenberg, O. Bunk, R. Johnson, R. Feidenhans'l, and M. Nielson, Surf. Sci. **414**, 254 (1998).
[12] L. Bardotti, P. Jensen, A. Hoareau, M. Treilleux, B. Cabaud, A. Perez, and F. Cadete Santos Aires, Surf. Sci. **367**, 276 (1996).
[13] R. Anton and I. Schneidereit, Phys. Rev. B **58**, 13874 (1998).
[14] J. Arthur and A. Cho, Surf. Sci. **36**, 641 (1973).
[15] A. Koma, K. Sunouchi, and T. Miyajima, J. Vac. Sci. Technol. B **3**, 724 (1985).
[16] P. Jensen and X. Blase, Phys. Rev. B **70**, 165402 (2004).
[17] M. Atashbar, D. Banerji, S. Singamaneni, and V. Bliznyuk, Nanotechnology **15**, 374 (2004).
[18] E. Walter, B. Murray, F. Favier, G. Kaltenpoth, M. Grunze, and R. Penner, J. Phys. Chem. B **106**, 11407 (2002).
[19] R. Anton and P. Kreutzer, Phys. Rev. B **61**, 16077 (2000).
[20] S. Granjeaud, K. Yckache, M. Dayez, A. Humbert, C. Chapon,

and C. Henry, Microsc. Microanal. Microstruct. **4**, 409 (1993).
[21] G. Francis, L. Kuipers, J. Cleaver, and R. Palmer, J. Appl. Phys. **79**, 2942 (1996).
[22] T. A. Witten and L. M. Sander, Phys. Rev. B **27**, 5686 (1983).
[23] J. Metois, J. Heyraud, and Y. Takeda, Thin Solid Films **51**, 105 (1978).
[24] A. Schwartz, M. Kumar, and B. Adams, *Electron Back Scatter Diffraction in Materials Science* (Plenum, New York, 2000).
[25] H. Wang, J. Jing, and P. Henriksen, J. Vac. Sci. Technol. A **11**, 1987 (1993).
[26] J. Donohue, *The Structures of the Elements* (Wiley, New York, 1974).
[27] F. Jona, Surf. Sci. **8**, 57 (1967).
[28] S. A. Scott, M. V. Kral, and S. A. Brown, Surf. Sci. **587**, 175 (2005).
[29] C. Chapon, S. Granjeaud, A. Humbert, and C. Henry, Eur. Phys. J.: Appl. Phys. **13**, 23 (2001).
[30] Z. Zhang and M. Lagally, Science **276**, 377 (1997).
[31] J. Rogowksa, Vacuum **74**, 153 (2004).
[32] W. Mullins and R. Sekerka, J. Appl. Phys. **34**, 323 (1963).
[33] C. Jeffrey, D. Harrington, and S. Morin, Surf. Sci. **512**, L367 (2002).
[34] S. A. Scott, M. V. Kral, and S. A. Brown (unpublished).
[35] B. Stegemann, C. Ritter, B. Kaiser, and K. Rademann, J. Phys. Chem. B **108**, 14292 (2004).
[36] R. Schwoebel and E. Shipsey, J. Appl. Phys. **37**, 3682 (1966).
[37] L. Gavioli, K. R. Kimberlin, M. C. Tringides, J. F. Wendelken, and Z. Zhang, Phys. Rev. Lett. **82**, 129 (1999).
[38] R. Otero, A. L. Vázquez de Parga, and R. Miranda, Phys. Rev. B **66**, 115401 (2002).
[39] J. Sadowski *et al.*, AIP Conf. Proc. **696**, 738 (2003).
[40] M. Saito, T. Ohno, and T. Miyazaki, Appl. Surf. Sci. **237**, 80 (2004).